Fatigue testing and the evolution of the defect microstructure in Si single crystals by transmission electron microscopy

Fatigue testing and the evolution of the defect microstructure in Si single crystals by transmission electron microscopy

M Legros, O Ferry, J-P Feiereisen, A Jacques and A George

Laboratoire de Physique des Matériaux, UMR 7556, Ecole des Mines, Parc de Saurupt, 54042 Nancy, France

Abstract

We performed fatigue testing of single-crystalline silicon in a temperature and strain rate domain where lattice friction is still effective: 800–900 °C and $(1.5–6) \times 10^{-4}$ s^{-1}. Tension–compression loading was applied under plastic strain amplitude control. For plastic strain amplitudes ranging from 6×10^{-4} to 10^{-2}, cyclic stress–strain curves exhibit two different stages of hardening and pass through a maximum before saturation is reached. At variance from what is observed in metals, the saturation and maximum stresses are decreased when the strain amplitude per cycle is increased. Microscopical observations suggest that strain localization takes place near the maximum cyclic stress and beyond. Several types of dislocation arrangement have been revealed by transmission electron microscopy observations. Before mechanical saturation, edge dislocation dipoles sit mainly in thick rectilinear walls. When observed perpendicularly, these walls form either linear or corrugated arrangements. Once the maximum stress is reached, it seems that part of the microstructure ceases to participate in the imposed deformation while other regions concentrate it. In the former case, the dislocation structure anneals and a loop structure is created from the dipolar walls. In the latter case, active dislocation walls condense in much thinner walls, similarly to what is observed in the persistent slip bands in face-centred cubic metals, but deformation bands in Si are much wider.

(Some figures in this article are in colour only in the electronic version)

1. Introduction

While the mechanical behaviour in fatigue and the corresponding dislocation structures have been widely investigated in the case of metals, almost no data are available for cyclic deformation of elemental semiconductors like Si or Ge.

In cyclic deformation under plastic strain amplitude control, the peak stress reached at the end of each half-cycle generally increases with testing time—i.e. number of cycles or

cumulative strain—up to a stable saturation level. In bcc metals, this saturation level was observed to increase monotonically with the plastic strain amplitude, γ_p [1]. In face-centred cubic (fcc) metals, the stress at saturation also increases with γ_p at low ($\gamma_p \leqslant 10^{-4}$) and high ($\gamma_p \geqslant 10^{-2}$) amplitudes, but remains constant in the middle range. This plateau was explained by the localization of strain in zones called persistent slip bands (PSBs). As γ_p is increased from $\sim 10^{-4}$ to $\sim 10^{-2}$, the volume occupied by PSBs increases until it fills the whole sample gauge (for reviews see [1–6]).

The dislocation patterning associated with the PSBs and the surrounding matrix has also been under focus. A persistent challenge is to understand how the 'hard' vein structure of the matrix can transform into the 'soft' ladder structure once a critical dislocation density is reached. The veins are made of dense and unorganized bundles of edge dislocation dipoles separated by channels containing a lower dislocation density. The ladder structure consists of much thinner dislocation walls, regularly spaced and oriented preferentially along the edge direction. Once the PSBs are formed, it is possible to link the interwall spacing in the ladder structure to the macroscopical saturation stress [7, 8].

These typical dislocation arrangements are much harder to evidence in bcc metals such as Fe [1, 9]. Moreover, in fcc alloys with low stacking fault energy (SFE), mechanical saturation is only reached at very small strain amplitude [10]. A question is whether the observed differences in mechanical behaviour and dislocation arrangements between fcc and bcc metals, with respect to strain localization and PSB formation, are imputable to the difference of slip geometry, of cross-slip ability or of lattice friction.

Combining the slip modes of fcc metals, a rather low SFE, comparable to that of Cu, and the large lattice friction which characterizes most bcc metals, silicon is an attractive material for fatigue experiments. The lattice friction does not, however, operate in the same manner in Si and bcc metals. In Si, dislocations tend to align in $\langle 110 \rangle$ directions, i.e. they have either screw or 60° character with comparable lattice friction on both types. Both planar slip and cross-slip are thermally activated, with different activation energies [11]. In bcc metals, only screws have a strong lattice friction, while edges are much more mobile [12].

The main reason why Si has only rarely been tested in fatigue is its brittleness at room temperature. The grip problem for tension/compression testing has proved very difficult to solve, and the only previous work was that of Scoble and Weissmann [13] who used a rotating bending jig essentially on Ge samples. This apparatus produced multi-slip activity and dislocation patterns that consisted essentially of misoriented cells with a very low density. No mechanical data (stress/strain) were reported.

We have recently shown that uniaxial tension/compression testing of single-crystalline Si was feasible under strain amplitude control [14]. Dislocations with a low density were found to be arranged in cells in the primary glide plane or in clusters when viewed end on. This indicated that a significant increase of the cumulative strain was needed to favour dislocation–dislocation interactions and eventually reach fatigue-type patterning. More recently, a PSB-like structure was observed in Si cycled to a large number of cycles [15]. However, it has been pointed out that the ladder structure may not be as common in Si as in fcc metals and that new dislocation patterns may be more representative. The aim of this paper is to analyse some of these structures in relation to the measured mechanical properties of Si in fatigue, between 825 and 900 °C where the lattice friction remains significant.

2. Experimental details

The shape and preparation of tension/compression samples used in this study are described in more detail elsewhere [15, 16]. Single-slip conditions on the $(11\bar{1})$ [011] system are
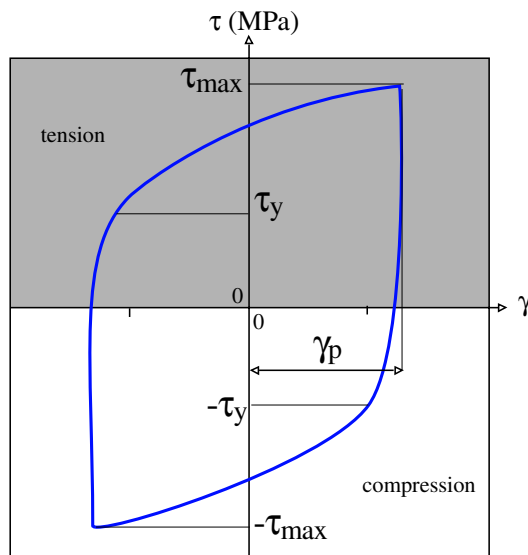
Figure 1. Typical tension/compression hysteresis cycle: the resolved shear stress τ is plotted against the resolved plastic strain γ (the elastic strain is subtracted). γ_p is the strain amplitude per cycle, τ_y represents the yield stress and τ_{max} the maximum stress for each cycle.

obtained by machining the pure FZ Si single crystals along a [231] axis. Surface flaws were removed by careful mechanical and chemical polishing. Mechanical testing was performed in a hydraulic MTS straining system equipped with a Centorr furnace, under a low pressure Ar/He atmosphere. The sample heads were strongly tightened in compression within the specially designed graphite grips in order to avoid loss of contact at stress reversals, even under maximum applied stress conditions. The success of experiments was strongly dependent on the quality of the specimen surface polishing and on the alignment of the whole sample–grips–testing system assembly.

All experiments started with a pre-straining treatment of a few tens of cycles (typically up to ~10% cumulative strain) at 980 °C, in order to develop a dislocation density high enough to allow further straining at a lower temperature (i.e. at higher stress). The cycle amplitude and strain rate applied during this pre-straining were respectively 8×10^{-4} and 4×10^{-4} s^{-1}. The aim of this treatment was to suppress the characteristic yield peak behaviour of dislocation-free Si, and thus to decrease the risk of brittle failure at the beginning of the test.

The sample was then cooled down to the desired testing temperature under residual load. Cycling was initiated by increasing the strain amplitude until the nominal amplitude was reached. About ten cycles are necessary to complete this transition. The strain amplitude control routine was custom written under Lab View® and the crosshead position was permanently computer controlled and adjusted to keep the plastic strain rate $\dot{\gamma}_p$ as constant as possible during each cycle. To ensure the shortest elastic loading, a periodic triangular-shaped signal was applied to the value ($\Delta l - F/E$) where Δl is the measured strain, F the measured force and E the apparent Young modulus of the system, as measured during pre-straining. The rate of acquisition/command between the computer and the testing machine was 1000 data lines s^{-1} independently of the cycle period. Several other routines and numerical noise reduction filters were added to minimize short oscillations that appeared during the test, especially at the transitions between tension and compression half cycles. A tension/compression cycle is
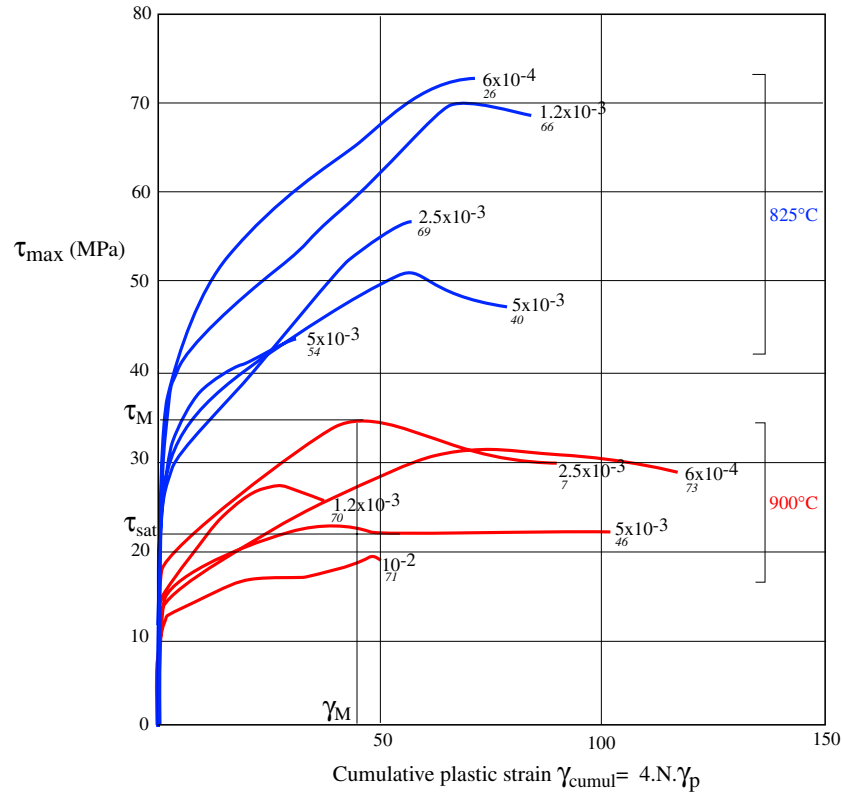
Figure 2. Evolution of τ_{max} versus γ_{cumul} (cyclic hardening curves) at different plastic strain amplitudes γ_p (noted at the end of each curve) and for two temperatures: $T = 825\,°C$ (thin curves) and $T = 900\,°C$ (thick curves). The number written in italics under γ_p is the specimen number. τ_M, which is the maximum value of τ_{max}, and γ_M, which is the value of γ_{cumul} at which τ_M occurs are marked for sample 7. Saturation stress, τ_{sat}, is marked for sample 46. For all the hardening curves, $\dot{\gamma}_p = 3 \times 10^{-4}\,\mathrm{s}^{-1}$.

shown in figure 1. The data line acquired throughout the entire test consisted of the machine cross-head position, the strain Δl and the force F.

Over each tension/compression cycle, the yield stress τ_y is followed by a hardening stage with a rate of about $\mu/100$(μ: shear modulus) to a peak stress, τ_{max} attained for $\gamma = \gamma_p$. As cycling continues, the evolution of τ_y and τ_{max} were monitored as a function of the number of cycles N or the cumulative plastic strain $\gamma_{cumul} = 4N\gamma_p$ (figure 2). Although τ_{max} was consistently observed to be slightly larger in compression before and around the maximum τ_M (see figure 2) and slightly larger in tension in the saturation range, the values of τ_{max} given hereafter are averaged between τ_{max} (tension) and $-\tau_{max}$ (compression). To date, more than 70 tests have been performed and 26 completed. The completed tests that are reported here allowed us to investigate four temperatures from 825 to $900\,°C$ with $25\,°C$ intervals and five strain amplitudes γ_p, ranging from 6×10^{-4} to 10^{-2}.

All the results presented here were obtained with the same strain rate of $3 \times 10^{-4}\,\mathrm{s}^{-1}$. Note that $\gamma_p = 6 \times 10^{-4}$ is close to the minimum plastic strain amplitude that we are able to reach with the present mechanical testing set-up.

After mechanical testing, the sample surface was examined by optical microscopy and SEM. Slices with a normal parallel to $[11\bar{1}]$ or $[2\bar{1}1]$ were cut using a diamond wire saw.

The $[11\bar{1}]$ foil normal corresponded to an orientation parallel to the primary slip plane. The $[2\bar{1}1]$ foil normal corresponded to an orientation perpendicular to the primary slip plane and containing the primary Burgers vector $b_1 = 1/2$ [011]. TEM thin foils with large observable areas were prepared with the tripod polishing technique. TEM observations were performed on a Philips CM200 microscope operating at 200 kV.

3. Experimental results

3.1. Mechanical behaviour

As mentioned before, both τ_y and τ_{max} were monitored during the test. The evolution of τ_y versus γ_{cumul} ($\gamma_{cumul} = 4N\gamma_p$) showed very little variation throughout a complete test [16]. The evolution of τ_{max} versus γ_{cumul} (cyclic hardening curve) is given for five different plastic strain amplitudes at 900 and 825 °C (figure 2). Similar data collected at 850 and 875 °C and hardening curves realized at different strain rates or at 800 °C are not presented here. In all the cases, τ_{max} showed the typical progression represented in figure 2.

With increasing γ_{cumul}, τ_{max} increased first logarithmically up to $\gamma_{cumul} \approx$ 5–10 and then linearly. This linear hardening stage lasted longer for small γ_p. For a given strain rate, the hardening rate of the linear portion was shown to depend on γ_p and on temperature [16]. At the end of the linear hardening, τ_{max} reached a maximum, hereafter called τ_M. This maximum, that can be smooth (sample 73, figure 2) or sharper (sample 7), is followed by a decrease of τ_{max}. On tests that were carried on longer, a saturation stress τ_{sat} was eventually reached. The mechanical decrement following τ_M saturation was observed to be weak (sample 46, figure 2) or more marked (sample 7). No clear relation was found between γ_p and the sharpness of τ_M or the following decrease of τ_{max}. It seemed, however, that intermediate γ_p (10^{-3}–2.5×10^{-3}) gave a sharper τ_M and a larger τ_{max} decrement. As can be seen on several curves (samples 26, 54, 69 or 70 for example) the tests were interrupted before a decrease of τ_{max} was observed. This suspension of cycling was needed to observe the dislocation microstructure corresponding to τ_M since some annealing could be seen in samples that were cycled well after τ_M was reached (see section 4). As expected in a domain where friction forces are active, decreasing temperature clearly shifts all the curves towards the upper stresses. Note that in the case of sample 71, a first maximum around $\gamma_{cumul} = 28$ is observed while τ_{max} continues to rise until $\gamma_{cumul} = 55$. After observation of the sample, it seems that the second hardening (observed only in compression) was caused by the significant activation of a secondary slip system. For this sample 71, the pertinent value of γ_M has thus been taken at the first maximum, e.g. $\gamma_M = 28$ (figure 3(b)). The effects of γ_p on the observed shift of τ_M in stress and γ_{cumul} are analysed in figure 3.

Figure 3(a) shows the variation of τ_M as a function of γ_p. For a given temperature, this curve is also known as the cyclic stress–strain (CSS) curve. The three curves obtained at 850, 875 and 900 °C show a decrease of τ_M with γ_p except for $\gamma_p = 2.5 \times 10^{-3}$ where the value of τ_M reaches a maximum. At 825 °C, the same global behaviour is observed but the maximum of τ_M is shifted towards the smallest γ_p, i.e. $\gamma_p = 6 \times 10^{-4}$. This CSS curve differs radically from what is observed in metals and a hypothesis to explain this discrepancy will be introduced in the discussion section.

In the same way that a larger γ_p seems to bring down τ_M, it also diminishes substantially γ_M, which is the value of the cumulative strain at which τ_M is reached (see figure 2). In figure 3(b) the evolution of γ_M as a function of γ_p is plotted. It appears clearly that between 850 and 900 °C the maximum cyclic stress τ_M is attained more rapidly when γ_p is increased. At 825 °C, this evolution is less marked but still exists.

Fatigue testing at lower temperatures and smaller γ_p failed because of too high stress levels. At 800 °C, one test at $\gamma_p = 10^{-2}$ was achieved. Investigating smaller plastic strain
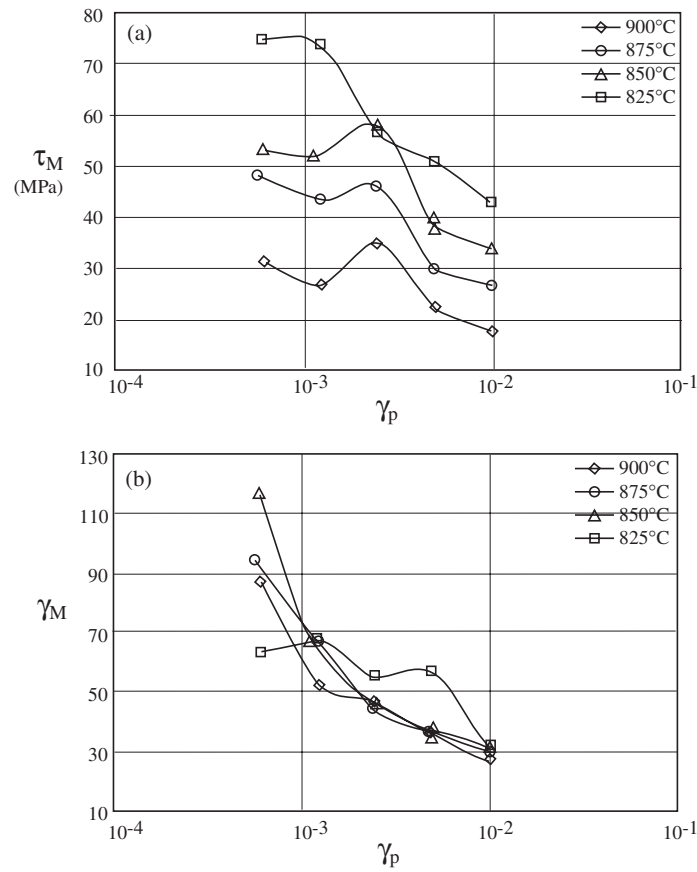
Figure 3. Evolution of the position of τ_M in stress (a) and cumulative plastic strain (b) as a function of γ_p. The curves in (a) are known as the CSS curves.

amplitudes is also difficult, due to the necessity to keep the plastic strain rate constant. Larger amplitudes than 10^{-2} and systematic strain rate variations have not been investigated so far.

3.2. Dislocation arrangements

One of the first goals of this study was to find out if strain localization happened in Si and what were the dislocation structures associated with this localization. As pointed out in an earlier work [16], SEM and optical surface observations of specimens deformed beyond τ_M pointed to non-crystallographic broad bands that did not fill the whole gauge circumference. These bands are made of thin lines parallel to the primary slip plane. In samples deformed at intermediate γ_p, the broad bands are 100–200 μm wide at their largest.

This paper will only address microstructures of samples that have been tested at $\gamma_p \leqslant 2.5 \times 10^{-3}$ (small amplitudes). TEM observations were made on foils with a $[11\bar{1}]$ or $[2\bar{1}1]$ normal (see section 2). Figure 4 combines two micrographs taken along these two orientations in a sample that broke before the maximum of the cyclic hardening stress–strain curves (τ_M, γ_M), i.e. in the linear hardening region. As can be seen in figure 4(a), the microstructure consists of dense dislocation walls separated by channels with a much lower density. These
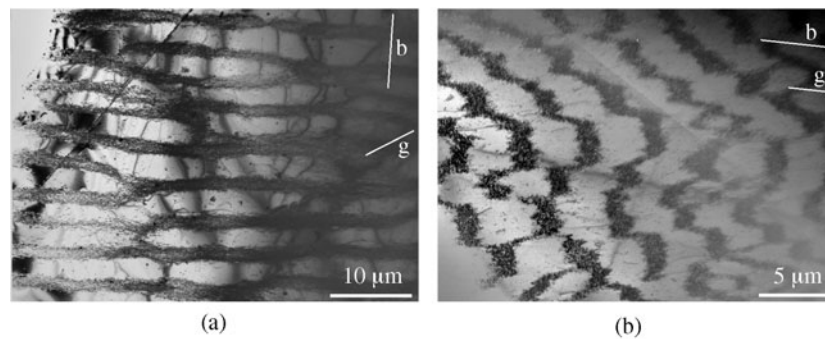
Figure 4. TEM bright field pictures taken in a sample (63) that did not reach mechanical saturation. Thin foils cut (a) parallel to the primary glide plane ($11\bar{1}$), foil normal FN = [$11\bar{1}$]; $b = a/2[0\bar{1}\bar{1}]$ is the primary Burgers vector, $g = 2\bar{2}0$; and (b) perpendicular to ($11\bar{1}$), FN = [$2\bar{1}1$], $g = 0\bar{2}\bar{2}$. $\gamma_{cumul} = 28$, $\gamma_p = 1.25 \times 10^{-3}$, $T = 825\,^{\circ}$C, $\dot{\gamma}_p = 3 \times 10^{-4}$ s^{-1}.

walls are aligned along [$2\bar{1}1$], which means that they are perpendicular to the primary Burgers vector (edge character). Because these walls are very rectilinear and regularly spaced, they have been named 'stripes' [15]. The dislocation densities in both stripe walls and channels have been estimated to be 2×10^{11} and 5×10^8 cm^{-2} respectively [16]. In this case ($\gamma_{cumul} = 28$, $\gamma_p = 1.25 \times 10^{-3}$, $T = 825\,^{\circ}$C, $\dot{\gamma}_p = 3 \times 10^{-4}$ s^{-1}), the average and characteristic stripe wall width was 1.3 μm while channels were 2.6 μm wide.

Figure 4(b) was taken in a [$2\bar{1}1$] foil, which is the plane orientation perpendicular to the stripes in figure 4(a). This thin foil comes from the same specimen as figure 4(a). Dislocation edge dipoles are now viewed essentially end on. Corrugated dislocation walls with no clear crystallographic orientation are observed. The average wall and channel widths measured along [011] (primary Burgers vector) were found to be 1.4 and 2.9 μm, respectively. These values correspond well to the values found in the [$11\bar{1}$] orientation (parallel to the primary slip plane, figure 4(a)). It is however obvious that these values show an important scatter since they depend strongly on the exact location where measured. In the pictures, stripe walls can be as thick as 3.5 μm and as thin as 0.7 μm. Channel dimensions show a similar data spread.

Figure 5 regroups micrographs taken in a sample for which cycling was interrupted right after τ_M. The corrugated shape of the dislocation walls observed in figure 5(a) is similar to the structure visible in figure 4(b), with an average wall and channel width of 2.5 and 1.3 μm respectively. A closer inspection of the walls in figure 5(a) reveals a high density of loops instead of dipole segments. The other microstructure present in this sample is displayed in figure 5(b). It consists of thinner corrugated dislocation walls (0.4 μm along [011]) separated by channels that are as wide (1.3 μm) as in figure 5(a). The region in which these thin walls are observable extends over about 140 μm in the thin foil, which corresponds to the 100–200 μm wide broad bands observed optically on the surface. This suggests that the thin wall region could correspond to the strain localization and that this phenomenon takes place by 'condensation' of the initially thick walls. The transition zone between thick and thin walls is seen in figure 5(c). Figure 5(d) is a picture taken in a thin foil cut in the same sample with a [$11\bar{1}$] orientation. Dislocation walls appear as elongated braids, mostly of edge character. Compared to the stripe walls observed in figure 4(a), these braids are thinner and more sinuous. They are about 0.3–0.5 μm thick and are separated by 1.3–1.8 μm wide channels. These values coincide well with those obtained from figure 5(b), and strongly suggest that figures 5(b) and (d) are two different views of the same structure. In the TEM foil, braids spread over a region about 100×150 μm^2 wide while the rest of the observable area contains dislocation
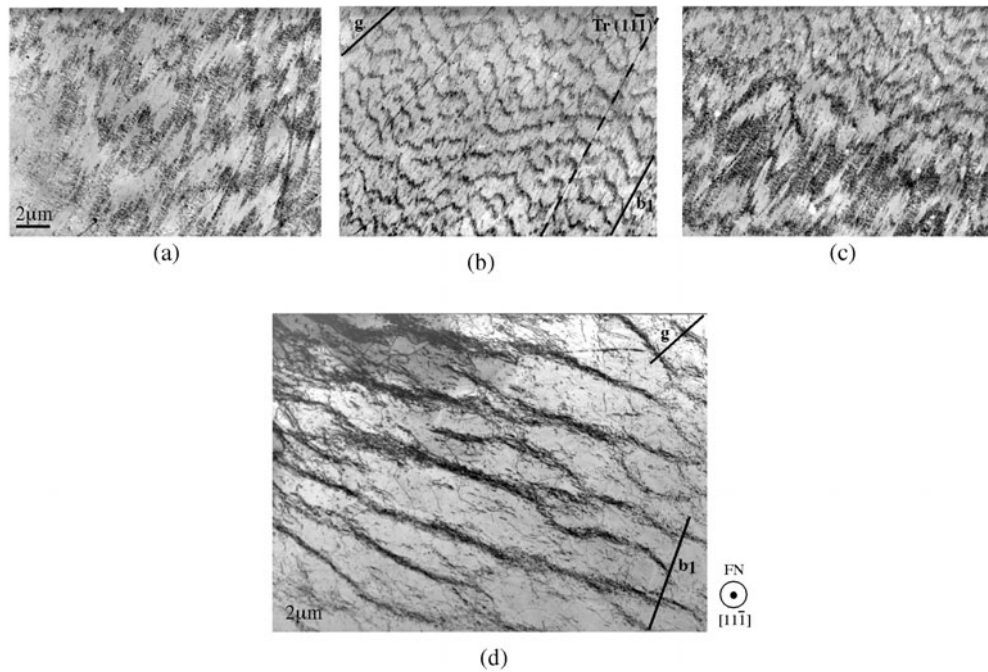
Figure 5. Dark field TEM pictures taken in a sample (26) that reached mechanical saturation (printed in reverse contrast). (a)–(c) Micrographs taken in foils with FN = [2$\bar{1}$1], showing respectively thick V-shaped walls, thin walls and the transition region between both microstructures. g = 111. (d) FN = [11$\bar{1}$], dislocations arranged in thin braids g = 040. γ_{cumul} = 71, $\gamma_p = 6 \times 10^{-4}$, $T = 825\,°C$, $\dot{\gamma}_p = 3 \times 10^{-4}\,s^{-1}$, $\tau_M = 74.5$ MPa, $\gamma_M = 65$.

loops (see figure 6) eventually organized in stripes. Elongated braids (figure 5(d)) would therefore correspond to the in-plane structure of condensed walls (figure 5(a)), while stripe walls (figure 4(a)) would correspond to thick corrugated walls (figures 4(b) and 5(a)).

When cycling is not stopped right after τ_M, another microstructure, consisting of dislocation loops and loop segments, becomes dominant. Figure 6(a) shows a region of a [11$\bar{1}$] foil containing these dislocation loops. As can be seen in this picture, some loops appear aligned along the primary Burgers vector. The measured dislocation density in this picture is 3×10^9 cm^{-2}. Figures 6(a) and (b) are taken in a region with a slightly lower density (10^9 cm^{-2}) with two different inclinations. Initially, most of these dislocations pertained to the (11$\bar{1}$) primary glide plane. When observed with a low tilt as in figure 6(b), the loops appear much thinner than when the foil is heavily tilted as in figure 6(c). This is evidence that they do not sit in their initial glide plane and are mainly prismatic. Observations made on [2$\bar{1}$1] foils taken from the same test sample confirmed the fact that these loops are prismatic. The presence of helix dislocation in figures 6(b) and (c) indicates that some climb processes are active.

4. Discussion

4.1. Mechanical behaviour

The shape evolution of the hysteresis stress–strain loops (figure 1) are sometimes used as an indication of a strain localization [17, 18]. As stated recently [16], we have not noticed such a variation of shape in Si. The strain localization may be better revealed by the peak in cyclic
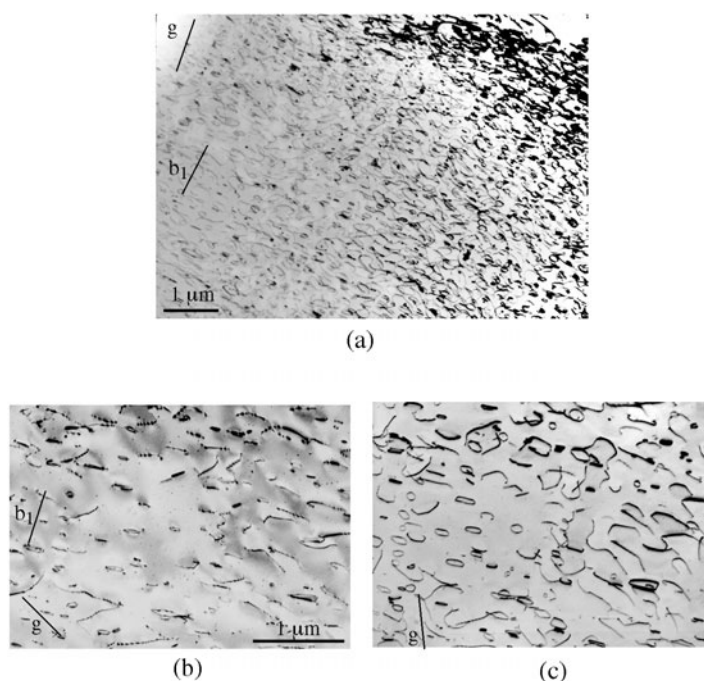
Figure 6. Dark field TEM pictures taken in a sample (58) that went beyond mechanical saturation (printed in reverse contrast). (a) Region of the foil containing a high density of loops. Note some loops aligned along b_1; (b), (c) dislocation loops in a zone of lower density. In (b), the foil is tilted $42°$ and $13°$ in (c). FN = $[11\bar{1}]$. (a) $g = 131$, (b) $g = \bar{2}0\bar{2}$, (c) $g = 00\bar{4}$. $\gamma_{cumul} = 56.5$, $\gamma_p = 2$; 5×10^{-3}, $T = 850\,°C$, $\dot{\gamma}_p = 3 \times 10^{-4}\ s^{-1}$, $\tau_M = 74.5$, $\gamma_M = 48$.

stress τ_{max} on the hardening curves (figure 2). The fact that τ_{max} reaches a maximum before decreasing as a function of γ_{cumul} has rarely been observed in the case of Cu, and only at large strain amplitudes [1] where the secondary dislocation fraction becomes significant [3]. In our case, this maximum is present over the whole range of strain amplitude investigated but seems more marked for the intermediate values of γ_p ($(1–2.5) \times 10^{-3}$). A similar effect is seen in figure 3(a) where the variation of τ_M versus γ_p displays a clear maximum for $\gamma_p = 2.5 \times 10^{-3}$. No clear microstructural explanation has been found so far for this peak that appears at 900, 875 and 850 °C. At 825 °C, the peak seems to be shifted towards the short strain amplitudes but an experiment at very low γ_p ($<6 \times 10^{-4}$) would be needed to confirm this hypothesis. At the present time, this is the lower limit of our experimental set-up.

As expected in a domain where lattice friction forces on dislocations are effective, stresses decrease rapidly with increasing temperature. At a given plastic strain amplitude and strain rate, this holds true for τ_y (see [16]), τ_{max} (figure 2), τ_M (figure 3(a)) and τ_{sat} (not shown). The exact physical meaning of this decrease has still to be specified since the dislocation mean free path during a half cycle, in these testing conditions, would be several times larger than the distances between dislocation walls [19, 20]. It is therefore clear that the travelling distance of edge dislocations—it is not so clear for screws—is limited by dislocation–dislocation interactions. In Cu, where friction forces are much weaker, the dependence of the saturation stress on the temperature also exists, but is less marked [21].

The most striking difference between fcc metals and Si lies in the CSS curve (figure 3(a)). In Cu, the CSS curve shows an increase of τ_{sat} with γ_p from 1.5×10^{-5} to 2×10^{-2} with a plateau extending from $\sim 10^{-4}$ to $\sim 10^{-2}$ [22]. In our case, except the noted peak at

$\gamma_p = 2 \times 10^{-3}$, τ_M shows a constant decrease at all the temperatures. Additional experiments where γ_{cumul} is taken far beyond γ_M would be needed to have a complete plot of τ_{sat} (instead of τ_M) versus γ_p. From the fragmentary data obtained so far, the CSS curve would look very similar. A partial explanation for this behaviour of τ_{sat} is to be found in figure 3(b) where the amount of cumulative plastic deformation γ_M needed to attain τ_M is drawn as a function of γ_p. γ_M becomes larger for small strain amplitudes, which means that the linear hardening seen in figure 2 lasted longer in term of cumulative strain or number of cycles. The reason for this faster saturation at high γ_p could be found in the higher proportion of non-reversible motion of dislocations at large plastic strains. In Cu, τ_{sat} is also attained faster when γ_p is increased, but the difference is much smaller and the saturation is always reached before $\gamma_{cumul} = 15$ [22].

Another reason for the decreasing of τ_{sat} as a function of γ_p could be the strain rate sensitivity of Si. If we assume that strain localization sets off at (γ_M, τ_M), the actual strain rate in deforming regions beyond γ_M will be larger than the imposed macroscopic value. This higher strain rate would call for a higher value of the measured stress. This hypothesis is coherent with the classic description of fatigue saturation in Cu where the fraction of deforming volume increases with γ_p. In the case of Si, the greater the volume fraction of active deformation, the less the actual strain rate and the less the observed stress. The non-exhaustive optical and SEM observations of the tested specimen may support this explanation, but the fact that τ_y does not show the same dependence as τ_M and τ_{sat} is arguable [16].

4.2. Dislocation structure

Over the whole temperature range investigated during this work, the observed dislocations consisted mainly of edge dislocation dipoles or multipoles arranged in bundles or walls. The basic elements of this microstructure are thus the same as the one encountered in fatigued metals, although the patterning is significantly different. Almost no screw or 60° dislocations, characteristic of monotonic straining at high stresses [23, 24], were found in the fatigued Si samples. Note that the cooling process from test temperature down to RT only freezes the microstructures, not the isolated dislocations.

The cyclic hardening curves of Si (figure 2) can be divided into four stages: a rapid hardening followed by a linear increase of τ_M, and a maximum followed by an asymptotic stress saturation. The first observations made in fatigued samples of Ge strained by bending [13], or in Si at high homologous temperature [14] reported low density cells. These structures compare rather well with our own ones, performed in a sample that failed below $\gamma_{cumul} = 10$ during the rapid hardening stage (not shown). The difference of dislocation density for the same amount of cumulative strain between Cu (that can be saturated at $\gamma_{cumul} = 10$) and Si (far from saturation) is noteworthy. This delayed saturation could be the result of the shortened mean free path of dislocations in Si, which results itself from the active lattice friction, but such an effect is not observed in bcc metals where friction forces are also present [3].

A notable increase in dislocation density develops during the linear hardening stage. The corrugated/stripe wall structure is found both in samples that reached τ_M (figure 5(a)) or failed in the linear hardening stage (figure 4). This arrangement may contain the maximum dislocation density, just before localization takes place. By analogy with Cu, we can consider this structure as the matrix, although the dislocation walls appear much more organized: neighbouring walls have similar shapes and width, and are separated by channels that are evenly wide. This periodicity also appears in the glide plane (figure 4(b)). The density in the stripe walls was estimated to be 2×10^{11} cm^{-2} [16], which is slightly lower than in Cu [3]. A similar matrix structure has also been observed in a previous work, surrounding ladder-like structures [15]. This ladder structure has not, however, been repeatedly observed in the subsequent TEM foils.

At least for the small strain amplitude, the strain localization in Si may be associated with corrugated thin walls (figure 5(b)) and braids (figure 5(d)). These structures are found only in samples that reached τ_M and they extend over tens of microns, as do the broad bands observed on the surface of test specimens. The average channel width is the same as in the matrix while the wall shape is maintained but with a thickness divided by two or three. This finding suggests that thin walls could be corrugated thick walls that have 'condensed' by a division mechanism shown in [16]. As in Cu, the transmission of dislocations between the thin (or condensed) walls would be easier than between the thick walls and most of the deformation has been carried out in these thin wall zones. When comparing the possible condensed structure in Si to the one found in Cu or Ni, it appears that the in-plane structures, made of sinuous braids of edge dislocations, are very similar, but the views perpendicular to the glide plane differ noticeably [22, 25]. In Si, the condensed wall regions extend over a hundred microns and are far from each other while PSBs are usually a few microns thick and dispersed in the matrix.

An important question is still open: at the transition between 'active' thin walls and 'inactive' thick walls (figure 5(c)), stress concentration should arise due to the strain incompatibility. The propagation of active bands parallel to the slip direction should deserve more detailed analysis.

Rows of prismatic closed loops are the third type of pattern found in fatigued Si that reached τ_M (figure 6). Most of these loops are prismatic and cannot have been created by simple dislocation glide. Some of these loops or segments are aligned along [011], but their diameter along the row is not constant, which rules out a Bardeen–Herring climb source mechanism. In addition to possible cross-slip processes, a significant amount of climb is needed to account for the formation of this structure. What these loops indicate is that the imposed deformation is no longer active in these regions. Foils cut in samples that went beyond γ_M contain either thin corrugated walls and thin braids or loop rows. These loop rows have densities that are much lower than in the stripes but, when cycling is stopped at τ_M, they possess a similar stripe pattern. Annealing a deformed Cu sample with a vein structure also showed the transformation of the matrix into dislocation loops with a lower density [26]. It is therefore reasonable to think that the thin walls concentrate the deformation while the matrix anneals out into these loops.

5. Conclusion

Mechanical data and microscopical observations showed that some strain localization occurs in Si over a wide range of parameters. This concentration of strain causes a drop in the hardening stress–strain curves. The cumulative plastic strain at which this maximum occurs is larger for small plastic strain amplitudes.

At small amplitudes, this maximum may be characterized by a condensation of thick corrugated dislocation walls. The walls that may appear by condensation of a structure initially composed of thick corrugated walls into thinner walls suggest that localization happens in a similar way than in PSBs in fcc metals. The dislocation patterns present however some significant differences and point out a possible role of cross-slip mechanisms. The relative cross slip and planar glide ability are different in Si or in metals; both processes are thermally activated in Si. Finally, the observed annealing processes in Si were diffusion assisted while edge dipole recombination in metals is more a matter of structural instabilities.

References

[1] Magnin T 1991 *Mem. Etud. Sci. Rev. Metall.* **88** 33
[2] Winter A T 1974 *Phil. Mag.* **30** 719

[3] Grosskreutz J C and Mughrabi H 1975 *Constitutive Equations in Plasticity* ed A S Argon (Cambridge, MA: MIT Press) p 251

[4] Laird C 1975 *Treatise on Materials Science and Technology* vol 6, ed R J Arsenault (New York: Academic) p 101

[5] Pedersen O B 1990 *Acta Metall. Mater.* **38** 1221

[6] Pedersen O B 1996 *Phil. Mag.* A **73** 829

[7] Brown L M 2000 *Mater. Sci. Eng.* A **285** 35

[8] Mughrabi H 2001 *Mater. Sci. Eng.* A **309/310** 327

[9] Sommer C, Mughrabi H and Lochner D 1998 *Acta Mater.* **46** 1527

[10] Wang Z, Gong B and Wang Z G 1999 *Acta Mater.* **47** 307

[11] George A 1997 *Mater. Sci. Eng.* A **233** 88

[12] Louchet F 1980 *Dislocations et Déformation Plastique-Yravals 1979* ed P Groh, L Kubin and J-L Martin (Location: Editions de Physique) p 149

[13] Scoble W R J and Weissmann S 1973 *Cryst. Lattice Defects* **4** 123

[14] Degli-Esposti J, Jacques A and Georges A 1997 *Mater. Sci. Eng.* **234–236** 1000

[15] Legros M, Jacques A and George A 2001 *Mater. Sci. Eng.* A **309/310** 233

[16] Legros M, Jacques A and George A 2002 *Phil. Mag.* A at press

[17] Pedersen O B and Winter A T 1982 *Acta Metall.* **30** 711

[18] Jin N Y 1989 *Acta Metall.* **37** 2055

[19] George A and Champier G 1979 *Phys. Status Solidi* c **53** 529

[20] Imai M and Sumino K 1983 *Phil. Mag.* A **47** 599

[21] Lisiecki L L and Pedersen O B 1990 *Acta Metall. Mater.* **39** 1449

[22] Mughrabi H 1978 *Mater. Sci. Eng.* **33** 207

[23] Oueldennaoua A 1983 *Thesis* Institut National Polytechnique de Lorraine

[24] Allem R 1986 *Thesis* Institut National Polytechnique de Lorraine

[25] Mecke K and Blochwitz C 1982 *Cryst. Res. Technol.* **17** 743

[26] Tabata T, Fujita H, Hiraoka M-A and Onishi K 1983 *Phil. Mag.* A **47** 841